

The impact of new (α , n) reaction rates on the weak s-process in metal-poor massive stars

WENYU XIN ^{1,2,3} CHUN-MING YIP ^{4,5} KEN'ICHI NOMOTO ⁶ XIANFEI ZHANG ^{1,2} AND SHAOLAN BI ^{1,2}

¹*Department of Astronomy, Beijing Normal University, Beijing 100875, China*

²*Institute for Frontiers in Astronomy and Astrophysics, Beijing Normal University, Beijing 102206, China*

³*National Astronomical Observatories, Chinese Academy of Sciences, Beijing 100101, China*

⁴*Department of Physics and Institute of Theoretical Physics, The Chinese University of Hong Kong, Shatin, N.T., Hong Kong S.A.R., People's Republic of China*

⁵*GSI Helmholtzzentrum für Schwerionenforschung, Planckstraße 1, D-64291 Darmstadt, Germany*

⁶*Kavli Institute for the Physics and Mathematics of the Universe (WPI), The University of Tokyo Institutes for Advanced Study, The University of Tokyo, Kashiwa, Chiba 277-8583, Japan*

Submitted to ApJ on April 24, 2025

ABSTRACT

Massive stars are significant sites for the weak s-process (ws-process). ^{22}Ne and ^{16}O are, respectively, the main neutron source and poison for the ws-process. In the metal-poor stars, the abundance of ^{22}Ne is limited by the metallicity, so that the contribution of $^{22}\text{Ne}(\alpha, n)^{25}\text{Mg}$ reaction on the s-process is weaker. Conversely, the $^{17}\text{O}(\alpha, n)^{20}\text{Ne}$ reaction is more evident in more metal-poor stars due to the most abundant ^{16}O in all metallicities. In this work, we calculate the evolution of four metal-poor models ($Z = 10^{-3}$) for the Zero-Age Main-Sequence (ZAMS) masses of $M(\text{ZAMS}) = 15, 20, 25,$ and $30 M_{\odot}$ to investigate the effect of reaction rates on the ws-process. We adopt the new $^{17}\text{O}(\alpha, n)^{20}\text{Ne}$ and $^{17}\text{O}(\alpha, \gamma)^{21}\text{Ne}$ reaction rates suggested by Wiescher et al. (2023) and $^{22}\text{Ne}(\alpha, n)^{25}\text{Mg}$ and $^{22}\text{Ne}(\alpha, \gamma)^{26}\text{Mg}$ from Best et al. (2013). The yields of the s-process isotope with updated reaction rates are compared with the results using default reaction rates from JINA REACLIB. We find that the new $^{17}\text{O}+\alpha$ reaction rates increase the ws-process mainly in all the stages, while the new $^{22}\text{Ne}+\alpha$ reaction rates only increase the ws-process in C and Ne burning stages. Updating these new reaction rates would increase the production of ws-process isotopes by tens of times. We also note that for more massive stars, the enhancement by new $^{17}\text{O}+\alpha$ reaction rates become more significant.

Keywords: massive stars, metal-poor stars, s-process, nuclear reactions

1. INTRODUCTION

Massive stars play a crucial role in the galactic chemical evolution. They synthesize the elements up to the iron group through charged-particle reactions during thermonuclear burning. Additionally, these stars are instrumental in produce elements heavier than iron via neutron capture processes. Then, all the elements produced

outside of the compact core are ejected into the environment by the supernova (SN) explosion.

Massive stars with Zero-Age Main-Sequence (ZAMS) masses of $M(\text{ZAMS}) \geq 12 M_{\odot}$ serve as significant sites for the weak s-process (ws-process) nucleosynthesis, which is responsible for producing isotopes with atomic masses around 65 to 90 (Kappeler et al. 1989). Early research predominantly associated the ws-process with the core He burning phase (Couch et al. 1974; Arnett & Thielemann 1985; Langer et al. 1989; Prantzos et al. 1990; Baraffe et al. 1992; The et al. 2000). Subsequent studies revealed that a significant secondary production

phase occurs during shell C burning, characterized by higher temperatures and neutron densities (Raiteri et al. 1991a, 1992, 1993; The et al. 2007). The isotopes synthesized during the shell C burning phase are crucial, as they are ejected during supernova explosions, largely unaltered. Furthermore, recent calculations about the yields of the ws-process have been extended to the entire evolutionary history of the star, including explosive burning (Hoffman et al. 2001; Rauscher et al. 2002; Limongi & Chieffi 2003; Tur et al. 2009; Limongi & Chieffi 2018). Limongi & Chieffi (2003) and Tur et al. (2009) have shown that the yields of the ws-process are not strongly modified by the SN explosion.

Differing from the main s-process dominated by $^{13}\text{C}(\alpha, n)^{16}\text{O}$ in AGB stars, the neutrons in the ws-process are provided by $^{22}\text{Ne}(\alpha, n)^{25}\text{Mg}$ (Peters 1968; Couch et al. 1974; Prantzos et al. 1990; Raiteri et al. 1991b). The available ^{22}Ne abundance in the core He burning is produced via $^{14}\text{N}(\alpha, \gamma)^{18}\text{F}(\beta^+\nu)^{18}\text{O}(\alpha, \gamma)^{22}\text{Ne}$. The ws-process is activated by $^{22}\text{Ne}(\alpha, n)^{25}\text{Mg}$ reaction once the temperature higher than 2.5×10^8 K ($T_9 = T/10^9\text{K} = 0.25$). During shell C burning, this reaction is re-activated by α produced by $^{12}\text{C}(^{12}\text{C}, \alpha)^{20}\text{Ne}$ channel (Arnett & Truran 1969).

^{22}Ne is primarily synthesized by the α -capture involving ^{14}N , which is derived from the initial metallicity of stars. Consequently, one would expect the yields of the ws-process elements to be low in metal-poor stars (Woosley & Weaver 1995; Baraffe et al. 1992). However, recent observations from Aoki et al. (2005, 2006); Chiappini et al. (2011) found that the ws-process elements in metal-poor stars are not as low as predicted. To account for this discrepancy, theoretical models have proposed that fast-rotating massive stars may enhance the production of the ws-process elements. In these models, rotation can promote the mixing of ^{14}N from the H-rich envelope into the convective core of He burning and increase the production (Chiappini et al. 2011; Frischknecht et al. 2012; Limongi & Chieffi 2018).

Additionally, some researchers have also explored the impact of uncertainties in the $^{17}\text{O}+\alpha$ reaction rate on the predicted yields of the ws-process elements (Baraffe et al. 1992; Hirschi et al. 2008). As the most abundant isotope, ^{16}O acts as a significant neutron poison through $^{16}\text{O}(n, \gamma)^{17}\text{O}$ reaction at the end of core He burning (Pignatari et al. 2010). Specifically, some neutrons are released again through the $^{17}\text{O}(\alpha, n)^{20}\text{Ne}$ reaction, while neutrons are not released from the $^{17}\text{O}(\alpha, \gamma)^{21}\text{Ne}$ reaction. In the metal-poor stars, the neutrons released by $^{22}\text{Ne}(\alpha, n)^{25}\text{Mg}$ reaction is limited, but neutron capture by ^{16}O remains significant, as ^{16}O is abundant across

all metallicities. Recent studies focused on the effects of $^{17}\text{O}+\alpha$ in the rotating stars (Frischknecht et al. 2012; Nishimura et al. 2017; Choplin et al. 2018). However, few studies have compared the effect of $^{17}\text{O}+\alpha$ with that of $^{22}\text{Ne}+\alpha$ in non-rotation metal-poor stars.

In this study, we investigate the standard ws-process in non-rotating stars, specifically comparing these new reaction rates suggested in recent references with those in JINA REACLIB. We will evaluate the implications of these new reaction rates on the standard ws-process, emphasizing how variations in these rates can significantly influence nucleosynthesis. In Section 2, we present the parameters of our stellar models and compare the reaction rates from the new references with those from JINA REACLIB. In Section 3, we use a model with $M(\text{ZAMS}) = 25 M_\odot$ as an example to illustrate the evolution of metal-poor stars. We further compare the effects of the $^{17}\text{O}+\alpha$ and $^{22}\text{Ne}+\alpha$ reactions on nucleosynthesis in Section 4. Finally, we conclude the study in Section 6.

2. MODELS AND INPUT PHYSICS

We employ the Modules for Experiments in Stellar Astrophysics (MESA, version 12778; Paxton et al. 2011, 2013, 2015, 2018, 2019; Jermyn et al. 2023) to follow various nuclear burnings and the structure evolution in stars from ZAMS until the Fe core collapse, when the infall velocity of the Fe core reaches 10^3 km s^{-1} . We only focus on nucleosynthesis before the explosion, as the final explosion makes only a slight modification to the ws-process abundance (Tur et al. 2009),

We calculate the evolution of four metal-poor stellar models of $M(\text{ZAMS}) = 15, 20, 25,$ and $30 M_\odot$ with MESA. The trajectories of these models are utilized in the WinNet code to investigate the effects of reaction rates on the ws-process. For the $^{17}\text{O}+\alpha$ reactions, we incorporate both competing reactions, $^{17}\text{O}(\alpha, n)^{20}\text{Ne}$ and $^{17}\text{O}(\alpha, \gamma)^{21}\text{Ne}$ as reported by Wiescher et al. (2023). The reaction rates for $^{22}\text{Ne}+\alpha$, including both the (α, n) and (α, γ) reactions are updated according to Best et al. (2013). To assess the impact of these reactions, we compare four reaction recipes for each model, as listed in Table 1. The differences among these reaction rates will be discussed in Section 2.1. Most physical parameters are taken from Xin et al. (2025) with some changes clarified in Section 2.2. Section 2.3 will outline the setup within the WinNet code.

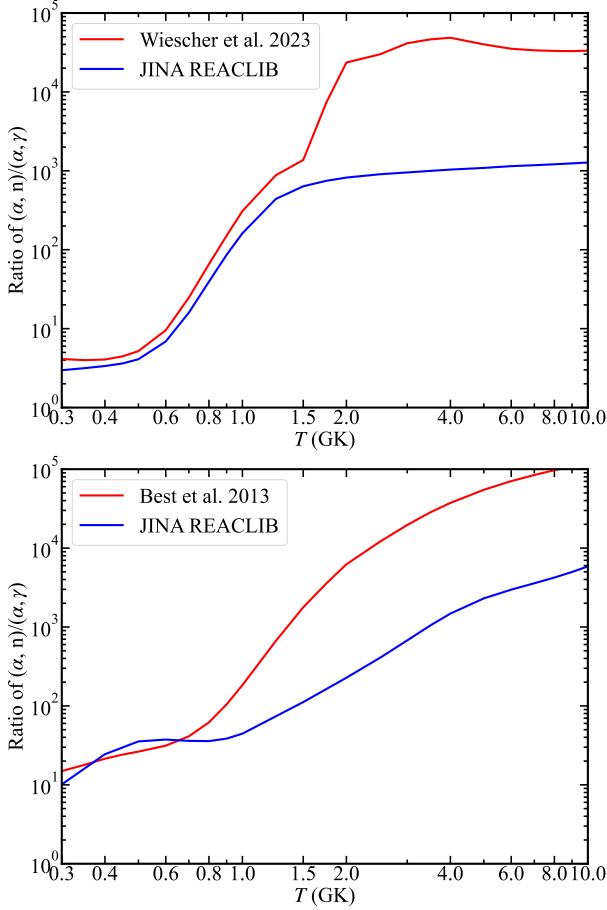
2.1. Reactions for Weak s-process

The $^{22}\text{Ne}(\alpha, n)^{25}\text{Mg}$ reaction is active at $T = 0.2$ GK and 1.0 GK in He and C shell burning shells, respectively. This reaction competes with $^{22}\text{Ne}(\alpha, \gamma)^{26}\text{Mg}$,

Table 1. The reaction recipes used in this work.

Case	$^{17}\text{O}+\alpha$	$^{22}\text{Ne}+\alpha$
1	REACLIB*	REACLIB
2	REACLIB	Wiescher et al. (2023)
3	Best et al. (2013)	REACLIB
4	Best et al. (2013)	Wiescher et al. (2023)

* JINA REACLIB Cyburt et al. (2010).

**Figure 1.** The $(\alpha, n)/(\alpha, \gamma)$ ratio as a function of temperature for $^{22}\text{Ne}+\alpha$ (top) and $^{17}\text{O}+\alpha$ (bottom) reactions.

which consumes ^{22}Ne without releasing any neutrons. In these shells, ^{16}O is the most abundant isotope and acts as the main neutron poison through $^{16}\text{O}(n, \gamma)^{17}\text{O}$. Fortunately, the neutrons absorbed by ^{16}O can be released again via $^{17}\text{O}(\alpha, n)^{20}\text{Ne}$. Therefore, the availability of neutrons for the ws-process is determined by the $(\alpha, n)/(\alpha, \gamma)$ ratio for both $^{22}\text{Ne}+\alpha$ and $^{17}\text{O}+\alpha$ reactions.

In Figure 1, we show the $(\alpha, n)/(\alpha, \gamma)$ ratios for the $^{22}\text{Ne}+\alpha$ (top panel) and $^{17}\text{O}+\alpha$ (bottom panel) reactions as a function of the temperature. In the top panel,

the $(\alpha, n)/(\alpha, \gamma)$ ratio for $^{22}\text{Ne}+\alpha$, as recommended by Wiescher et al. (2023), is observed to be 1.2 to 2.0 times higher than the values provided by REACLIB below 1.5 GK, a range typically associated with He and C shell burning. Notably, this enhancement increases dramatically, reaching several tens of times above 1.5 GK.

In the bottom panel, the $(\alpha, n)/(\alpha, \gamma)$ ratio for the $^{17}\text{O}+\alpha$ reaction suggested by Best et al. (2013) is similar to REACLIB below 0.7 GK, where only He burns. However, this ratio rapidly increases to several tens of times in the C, Ne, and O layers. With these updated reaction rates, we anticipate an increase in the neutron release from ^{22}Ne while reducing neutron consumption by ^{16}O . Consequently, the yields of the ws-process isotopes are significantly enhanced.

2.2. Input Physics in MESA

Table 2. Nuclides included in the nuclear reaction network of mesa_161.net.

Element	A_{\min}	A_{\max}	Element	A_{\min}	A_{\max}
n	1	1	S	31	35
H	1	2	Cl	35	38
He	3	4	Ar	35	40
Li	7	7	K	39	44
Be	7	10	Ca	39	46
B	8	8	Sc	43	48
C	12	13	Ti	43	51
N	13	15	V	47	53
O	14	18	Cr	47	57
F	17	19	Mn	51	57
Ne	18	22	Fe	51	61
Na	21	24	Co	55	63
Mg	23	26	Ni	55	64
Al	25	28	Cu	59	64
Si	27	31	Zn	60	64
P	30	33			

⁸Be is not included.

To achieve the convergence of the model structures within approximately 10%, a nuclear network comprising at least 127 isotopes should be included (Farmer et al. 2016). In this work, we utilize a more extensive nuclear network (mesa_161.net) that incorporates additional neutron-rich isotopes. Table 2 lists all the isotopes in mesa_161.net. We adopt a metallicity of $Z = 0.1 Z_{\odot}$ and assume solar metallicity ratios based on the work of Anders & Grevesse (1989).

We have enhanced both the temporal and spatial resolutions to ensure the numerical convergence. The mass resolution is critical for accurately capturing changes in the stellar structure (Farmer et al. 2016; Farag et al. 2022). The parameter `max_dq` controls the maximum fractional mass of a cell in the model, and we set `max_dq=5d-4`, which results in over 3,500 cells in the model. We adopt a minimum diffusion coefficient of $D_{\min} = 10^{-2} \text{ cm}^2 \text{ s}^{-1}$ to ensure that the global mixing timescale ($\tau = L^2/D_{\min}$) is significantly longer than the lifetimes of the stellar models. This allows us to neglect the effects of global mixing and to smooth local composition gradients (Farag et al. 2022).

After C burning, the core structure becomes more complex because of multi-shell burning, with the central entropy being significantly influenced by shell burning (see Xin et al. (2025)). To achieve finer granularity during the evolution, we impose limits on the changes in the logarithm of the central density and temperature. Specifically, we set $\delta_{\log \rho_c} < 10^{-3}$ and $\delta_{\log T_c} < 2.5 \times 10^{-3}$. Additionally, we restrict the change in the mass fraction of isotopes with `dX_nuc_drop_limit= 3 × 10-2` and tightening this limit to `dX_nuc_drop_limit_at_high_T= 10-2` when $\log T_c > 9.45$.

2.3. Post-processing Calculation with WinNet

The detailed nucleosynthesis in the stellar models is computed in post-processing using an extensive nuclear reaction network code WinNet (Reichert et al. 2023). The network consists of about 2000 isotopes from neutron and proton to thorium ($Z = 90$). The reaction rates of (n, γ) , (n, p) , (p, γ) , (α, n) , (α, p) , (α, γ) , and their inverse reactions from the JINA REACLIB database (Cyburt et al. 2010) are included. Theoretical weak rates from Langanke & Martínez-Pinedo (2001), electron chemical potentials from Timmes & Arnett (1999), and screening corrections from Kravchuk & Yakovlev (2014) are used.

For each stellar model, we map the initial composition and time evolutions of temperature and density from the MESA simulation on trajectories. The nucleosynthesis calculation of these trajectories is performed until the onset of core-collapse at the center. The region inside the steepest-density jump is expected to collapse into a neutron star eventually and not contribute to the yield of the *ws*-process nucleosynthesis. The steepest density jump occurs at the most active burning shell and has been defined in Xin et al. (2025). We will describe briefly the MESA result (Xin et al. 2025) in Section 3.

3. PRE-CCSN EVOLUTION AND EXPLODABILITY

3.1. Evolution of Massive Stars

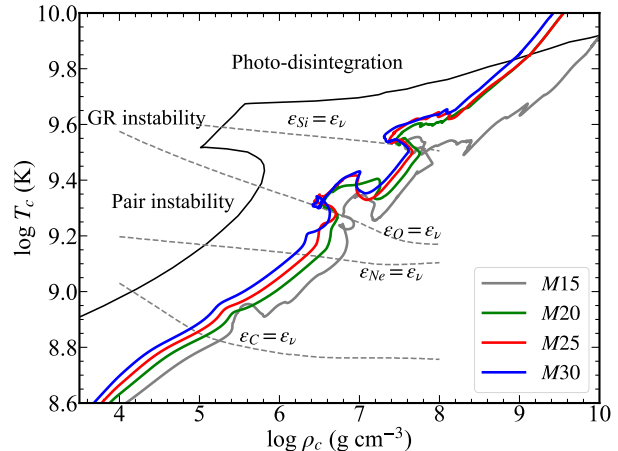


Figure 2. The central temperature against the central density for the evolution of stars with $M(\text{ZAMS}) = 15, 20, 25$ and $30 M_{\odot}$. The grey dashed lines show the ignition lines of C burning, Ne burning, O burning and Si burning, where the energy generation rate by nuclear burning equals the energy loss rate by neutrino emissions. In the region on the left of the black line, stars are dynamically unstable due to the electron-positron pair creation (indicated as “pair instability”) (Ohkubo et al. 2009), general relativistic effects (“GR instability”) (see, e.g., Osaki 1966), and the photo-disintegration of matter in nuclear statistical equilibrium (NSE) at $Y_e = 0.5$ (“photo-disintegration”) (Ohkubo et al. 2009).

After core He burning, the mass fraction of ^{12}C in the center is smaller for the smaller initial mass of the star. Only a star with $M(\text{ZAMS}) = 15 M_{\odot}$ can ignite convective C burning in the center, as it has sufficient fuel with $X(^{12}\text{C}) \sim 0.2$. In contrast, other models undergo contraction because the neutrino energy loss rate exceeds the energy production rate of C burning as shown in Figure 2. After Si burning, the star with $M(\text{ZAMS}) = 15 M_{\odot}$ exhibits a distinct behavior compared to other models because Si shell burning is energetic. However, the effects of Si shell burning are not the focus of this work and will be discussed elsewhere.

More massive stars eject more material but explode less frequently (Meyer et al. 1995). Considering the combined effects of ejected masses and event frequencies, stars with initial masses of $M(\text{ZAMS}) = 25 M_{\odot}$ are regarded as the most significant contributors to the chemical enrichment of galaxies (Weaver et al. 1978; Woosley & Weaver 1995). Therefore, we select the model of $M(\text{ZAMS}) = 25 M_{\odot}$ as a typical example for discussing stellar nucleosynthesis.

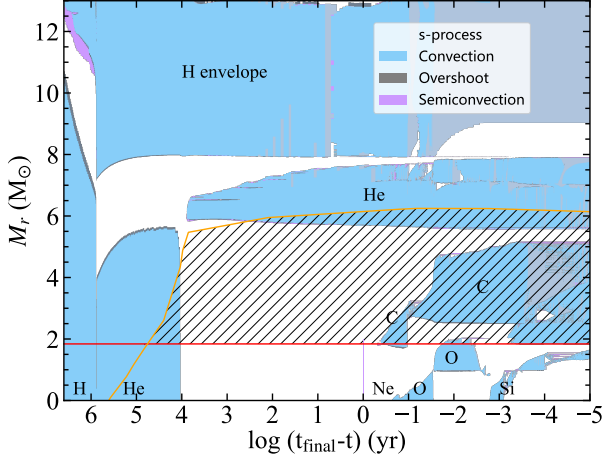


Figure 3. The Kippenhahn diagram of the star with $M(\text{ZAMS}) = 25 M_{\odot}$. The inner part of $M_r = 0 - 14 M_{\odot}$ is shown. The blue, grey, and pink represent the convection, overshoot, and semiconvection regions, respectively. The orange line is the isotherm line of 0.2 GK, and the red line shows the location of $M_r = 1.84 M_{\odot}$. Between these two lines, the hatched region indicates where the ws-process is taken into consideration.

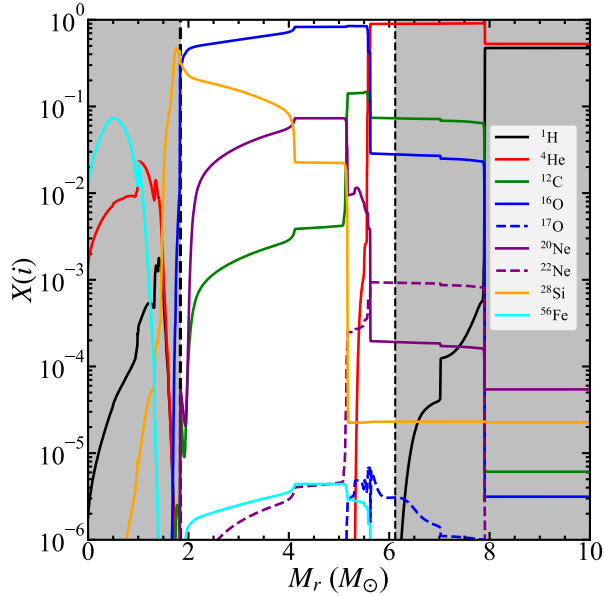


Figure 4. The mass distribution of the main isotopes from MESA. The two grey regions indicate where $M_r \leq 1.84 M_{\odot}$ and $T \geq 0.2$ GK.

In Figure 7, we present the Kippenhahn diagram for the star with $M(\text{ZAMS}) = 25 M_{\odot}$, tracking its evolution from H burning to Fe core collapse. The central temperature reaches approximately 0.2 GK at $\tau = t_{\text{final}} - t = 10^{5.6}$ yr. Here t is the time from ZAMS and t_{final} denote the time at the final stage of evolution, which is defined as the moment when the infall speed of the iron

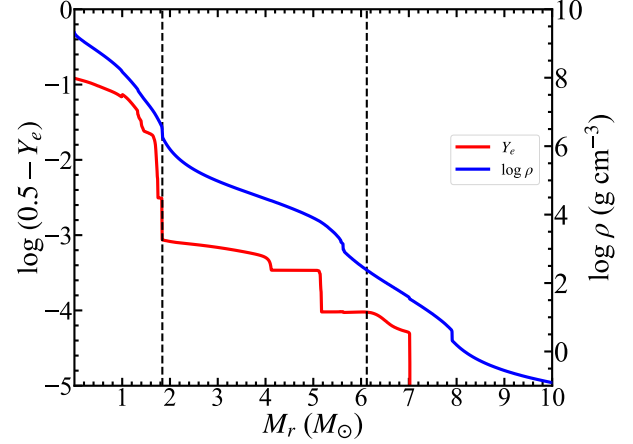


Figure 5. The mass distribution of the Y_e (red) and $\log \rho$ (blue). The two black lines indicate where $M_r = 1.84 M_{\odot}$ and $T = 0.2$ GK.

core reaches 1000 km s^{-1} . The orange line indicates the isotherm of $T = 0.2$ GK.

The ws-process is assumed to occur interior to this isotherm. After core He burning, this region extends to $M_r \sim 6.0 M_{\odot}$, and the He and CO core masses are 7.8 and $4.96 M_{\odot}$, respectively. C burning ignites off-center at $\tau = 10^{0.5}$ yr, nearly 3 years before the collapse. After $\tau = 10^{-3}$ yr (10 hours before collapse), shell C burning merges with shell O burning at $M_r = 1.84 M_{\odot}$, marking the location of the highest energy generation rate as indicated by the red line. The inner part of this region is predicted to form a proto-neutron star (PNS), while the outer layers are ejected. Therefore, this paper considers only the ws-process isotopes produced in the hatched region.

Figure 4 illustrates the mass distribution of the main isotopes at $t = t_{\text{final}}$. The ws-process region extends from the Si/O interface to the bottom of He burning shell, primarily composed of ^{16}O , ^{28}Si , ^{20}Ne , ^{12}C and ^4He . The mass fraction of seed isotopes “Fe” ranges from 10^{-4} to 10^{-5} . Additionally, the neutron excess, expressed as $\eta = 1 - 2Y_e$, of the ws-process region is observed to be $10^{-3} - 10^{-4}$, as shown in Figure 5. In the interior to $M_r = 1.84 M_{\odot}$, the neutron excess increases rapidly toward the center, reaching $\eta \sim 0.2$ in the center. This jump is primarily attributed to the reactions during O burning, including $^{16}\text{O}(^{16}\text{O}, n)^{31}\text{S}$ and the weak interactions such as $^{30}\text{P}(e^+, \nu)^{30}\text{S}$, $^{33}\text{S}(e^-, \nu)^{33}\text{P}$, $^{35}\text{Cl}(e^-, \nu)^{35}\text{S}$, $^{37}\text{Ar}(e^-, \nu)^{37}\text{Cl}$ (Woosley et al. 2002).

3.2. The Mass Cut

In Figure 5, significant jumps in both density and Y_e are observed near the mass coordinate $M_r = 1.84 M_{\odot}$. This layer corresponds to the base of the O burning

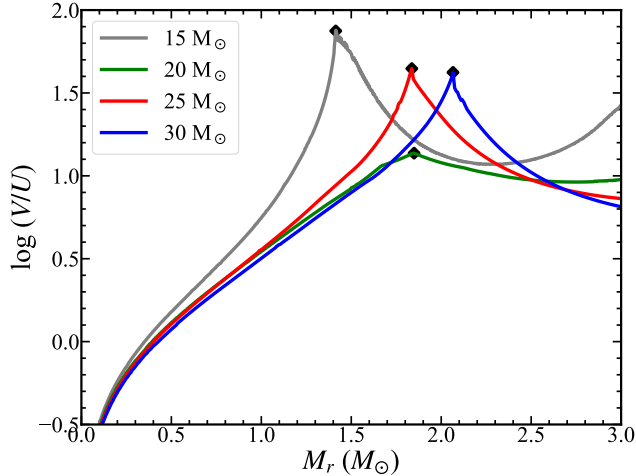


Figure 6. The mass distribution of $\log V/U$ at $\tau = t_{\text{final}}$. The orange diamonds are the location of M_4 , which is defined at the mass coordinate of specific entropy $s = 4 \text{ erg g}^{-1} \text{K}^{-1}$.

shell being the layer of the peak energy generation. To measure the strength of shell burning, we use V/U

$$\frac{V}{U} = -\frac{d \ln P}{d \ln M_r} = \frac{GM_r^2}{4\pi r^4 P} \quad (1)$$

where U and V are defined in earlier studies (Schwarzschild 2015; Hayashi et al. 1962; Sugimoto & Nomoto 1980; Kippenhahn et al. 2013).

As explained in detail in Xin et al. (2025). U relates to the degree of the density jump and V/U is the pressure gradient against M_r . The mass coordinate where V/U reaches its maximum is represented as $M(V/U_{\text{max}})$. The relation between V/U and the strength of shell burning is straightforward. When O shell burning is more energetic, it produces higher energy to prevent the contraction and even to cause the expansion of outer layers, This makes the gradients of entropy and pressure against M_r (i.e., V/U) larger.

Table 3. The final mass, He core mass, CO core mass and $M(V/U_{\text{max}})$ for each model. The $M(\text{He})$ and $M(\text{CO})$ are defined at the layers where $X(\text{H})$ and $X(\text{He})$ lower than 10^{-4} .

$M(\text{ZAMS})$	$M(\text{final})$	$M(\text{He})$	$M(\text{CO})$	$M(V/U_{\text{max}})$
M_{\odot}	M_{\odot}	M_{\odot}	M_{\odot}	M_{\odot}
15	14.88	4.66	2.39	1.41
20	19.79	6.25	3.85	1.85
25	24.73	7.80	4.96	1.84
30	29.50	9.86	6.76	2.07

Figure 6 shows the distribution of $\log V/U$ against M_r at $\tau = t_{\text{final}}$ for each model. We note that $M(V/U_{\text{max}})$ coincides with M_4 , i.e., M_r at a specific entropy of $s = 4 \text{ erg g}^{-1} \text{K}^{-1}$, being previously used for the mass cut which would divide the inner proto-neutron star (PNS) and the outer ejecta in the explosion (Woosley & Heger 2007; Heger & Woosley 2010; Sukhbold et al. 2016; Farmer et al. 2023). In the present study, we adopt $M(V/U_{\text{max}})$ as the mass cut, because it is the location of the steepest gradients of pressure and density (Xin et al. 2025). The core masses and $M(V/U_{\text{max}})$ for our models are listed in Table 3.

4. NUCLEOSYNTHESIS AND THE EFFECT OF REACTION RATES

4.1. The Nucleosynthesis in 25 M_{\odot} model

In this section, we present the results of the post-process nucleosynthesis and discuss the effects of updated reaction rates.

We selected a zone at $M_r = 2.3 M_{\odot}$ as a representative example to reveal the change in the mass fraction $X(i)$ of isotope i occurring during each burning stage after updating these reactions. $X(\text{Ga-Zr})$ and $X(\text{Nb-Th})$ are the cumulative mass fractions of isotopes from Ga to Zr ($A = 31 - 40$) and Nb to Th ($A > 40$), respectively. The reaction rates recipes used in Figure 7 (a - d) correspond to the cases 1 - 4 listed in Table 1. The chemical evolution of main isotopes is depicted in the top panel of Figure 7. The changes in $X(n)$ and ${}^4\text{He}$ for the default rates are displayed in the bottom panel of Figure 7 (a), while in Figure 7 (b) - (d), the value is normalized by $X_{\text{def}}(i)$ in Figure 7 (a) to stress the effect of these reaction rates. Table 4 lists the total mass fraction of the ‘‘Ga - Zr’’ elements in the initial abundance (X_{ini}), after He burning ($X_{\text{He-b}}$), C burning ($X_{\text{C-b}}$), and Ne burning ($X_{\text{Ne-b}}$). The data is visualised in Figure 8 by the ratios of ΔX to X_{ini} , ΔX is the change in the mass fraction in each burning stage.

Overall, these reaction rates significantly alter the production of the ‘‘Ga - Zr’’ elements rather than the ‘‘Nb - Th’’ elements. We thus focus on the ‘‘Ga - Zr’’ elements in this section. The initial value of $X(\text{Ga-Zr})$ is $X_{\text{ini}} = 7.87 \times 10^{-8}$. Enhancements of $X(\text{Ga-Zr})$ are observed 4 times at the end of He burning, the beginning of C burning, the end of C burning and Ne burning, respectively. They coincide with the neutron peaks and ${}^4\text{He}$ production in Figure 7.

After Ne burning, the total enhancement of $X(\text{Ga-Zr})$ is estimated by a ratio of $(X_{\text{Ne-b}} - X_{\text{ini}})/X_{\text{ini}}$, where $X_{\text{Ne-b}}$ and X_{ini} are listed in Table 4. Compared with X_{ini} ,

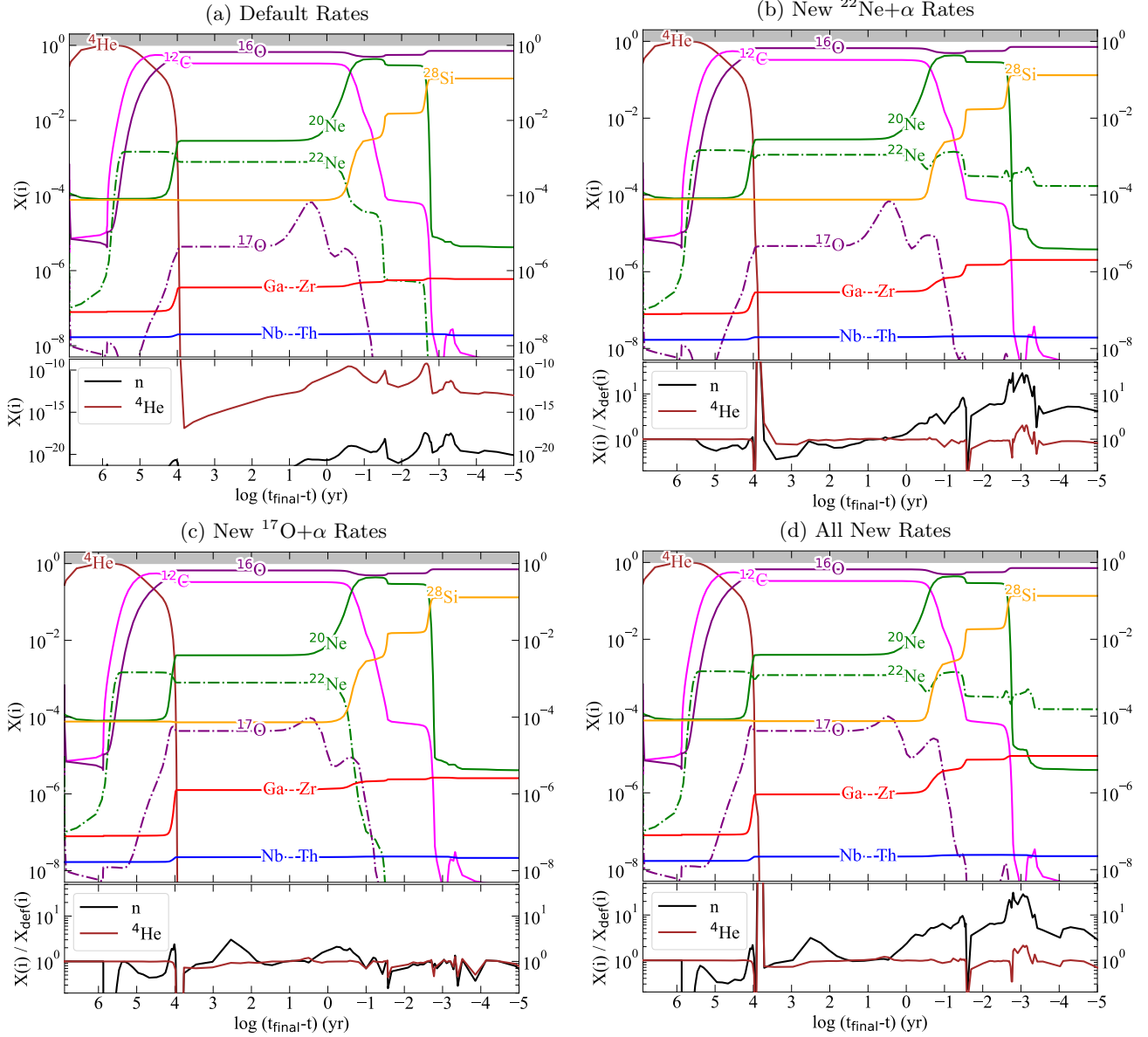


Figure 7. The chemical evolution in the OSi shell ($M_r = 2.3 M_\odot$). In the top panels of (a) - (d), changes in the mass fractions $X(i)$ of ${}^4\text{He}$, ${}^{12}\text{C}$, ${}^{16}\text{O}$, and ${}^{20}\text{Ne}$ show the burning stages. $X(\text{Ga} - \text{Zr})$ and $X(\text{Nb} - \text{Th})$ are the cumulative mass fractions of the s-process isotopes from Ga to Zr ($A = 31 - 40$) and Nb to Th ($A > 40$), respectively. In the bottom panel, the changes in $X_{\text{def}}(i)$ of neutrons and ${}^4\text{He}$ for the default rates are shown in (a). In (b) - (d) shown are the changes in the ratios $X(i)/X_{\text{def}}(i)$ between the “new” and default rates for n and ${}^4\text{He}$.

$X(\text{Ga-Zr})$ increases by a factor of 6.56, 23.77, 31.58 and 113.62 for (a) - (b), respectively. The forthcoming O burning will not enhance or even reduce their production because of more destruction at high temperatures (Tur et al. 2009).

When the default rates are used as in Figure 7 (a), the “Ga - Zr” elements are mainly synthesized during the He (51%) and C (41%) burning stages (see Figure 8). Only 8% of them are synthesized during the Ne burning stage because the main neutron source isotope ${}^{22}\text{Ne}$ is almost exhausted.

Table 4. The total mass fractions of the ws-process isotopes of $A = 31 - 40$ in the initial abundance, after He burning, C burning and Ne burning stages, respectively, in Figure 4.

Figure	X_{ini}	$X_{\text{He-b}}$	$X_{\text{C-b}}$	$X_{\text{Ne-b}}$
a	7.87E-08	3.42E-07	5.55E-07	5.95E-07
b	7.87E-08	2.87E-07	1.38E-06	1.95E-06
c	7.87E-08	1.21E-06	2.39E-06	2.56E-06
d	7.87E-08	9.34E-07	7.34E-06	9.02E-06

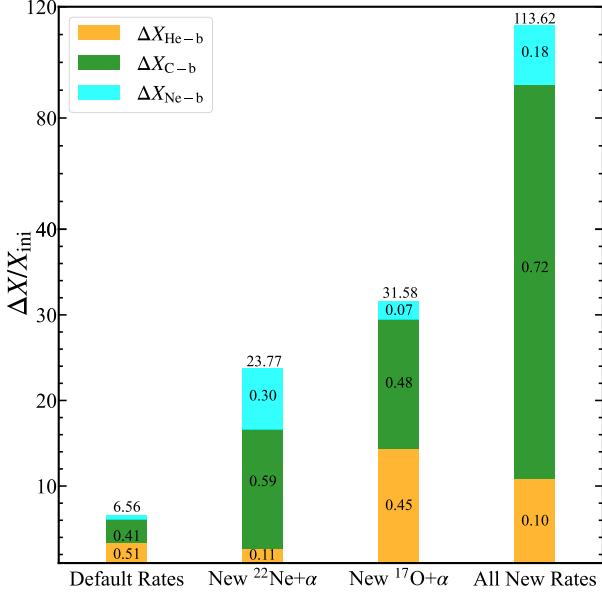


Figure 8. The total mass fraction of the ws-process isotopes from $A = 31 - 40$ after He, C, and Ne burning. All values are normalized by the initial abundance, $X_{\text{ini}} = 7.87 \times 10^{-8}$. The total value is written above each pillar and the contribution percentage of each burning stage is written in the center of the box.

With the new $^{17}\text{O}+\alpha$ reaction rates in Figure 7 (c), more than 93% of the “Ga - Zr” elements are synthesized during He and C burning stages, being similar to (a). The final X (Ga - Zr) is enhanced by a factor of 4.81 compared with default rates, Because both new $^{17}\text{O}(\alpha, n)^{20}\text{Ne}$ and $^{17}\text{O}(\alpha, \gamma)^{21}\text{Ne}$ reaction rates are lower than the default ones at temperatures below 0.7 GK (see Figure 15), $X(^{17}\text{O})$ reaches a higher level at the end of He burning with the new rates. When the temperature exceeds 0.7 GK, the ratio of $(\alpha, n)/(\alpha, \gamma)$ increases. Therefore, the new $^{17}\text{O}+\alpha$ reaction rates significantly enhance the production of the “Ga - Zr” elements at all stages, though only slightly altering their contribution percentages.

Comparing Figure 7 (a) and (b), the productions of the “Ga - Zr” elements are enhanced by a factor of 23.8 by using new $^{22}\text{Ne}+\alpha$ reaction rates, This is smaller than the increase in using the new $^{17}\text{O}+\alpha$ reaction rates. Since the new $^{22}\text{Ne}+\alpha$ rates are smaller than those in REACLIB (see Figure 14), ^{22}Ne is not exhausted until the core collapse. The $(\alpha, n)/(\alpha, \gamma)$ ratio of the new rates is 10 times higher than that of the default ones when the temperature exceeds 1.5 GK. A significant neutron rise is observed from six months before the explosion. As a result, almost 89% of the “Ga - Zr” elements are synthesized during C and Ne burning.

In Figure 7 (d), both the new $^{17}\text{O}+\alpha$ and new $^{22}\text{Ne}+\alpha$ reaction rates are updated. The production of the “Ga - Zr” elements are enhanced by more than one order of magnitude. But the contributions of He and Ne burning are only 10% and 18% and most of the “Ga - Zr” elements are synthesized during the C burning stage, which should alter the isotope composition of the “Ga - Zr” elements. Comparing (a, c) with (b, d), we can also note whether Ne burning contributes to the ws-process significantly, depending on the $^{22}\text{Ne}(\alpha, \gamma)^{25}\text{Mg}$ reaction rate. Only when this can some ^{22}Ne still exist during the Ne burning stage.

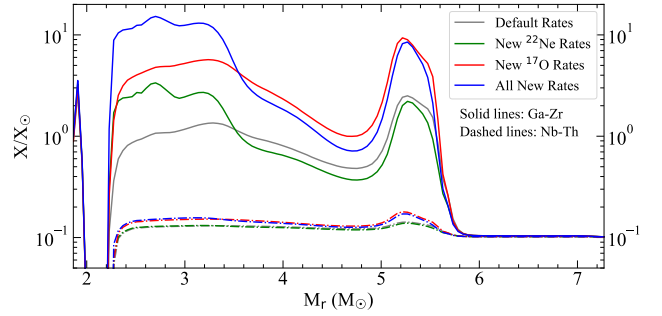


Figure 9. The abundance distributions of the ws-process elements at $M_r = 1.84 - 7.3 M_{\odot}$ in the He core of the $M(\text{ZAMS}) = 25 M_{\odot}$ star. The solid lines symbolize the “Ga - Zr” elements, while the dashed lines symbolize the heavier.

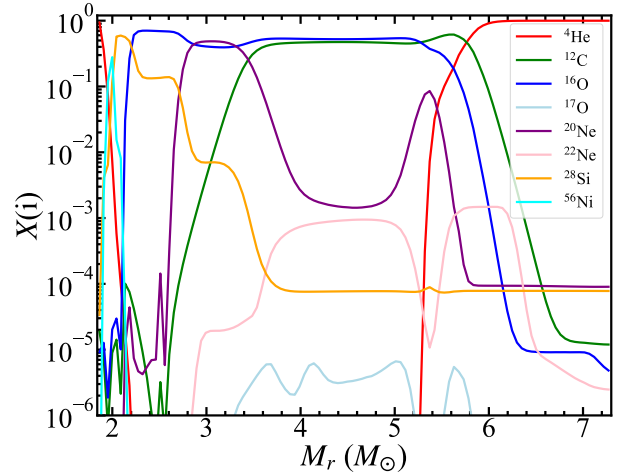


Figure 10. The distribution of the mass fractions of the main isotopes at $M_r = 1.84 - 7.3 M_{\odot}$ obtained from the post-processing calculation. Note that the mixing is not taken into consideration in the post-processing calculation because WinNet is a one-zone code. The comparison between this Figure and Figure 4 is made in Section 5.1.

Figure 9 displays the abundance distributions of s-process elements. We observe two distinct bumps in the abundance of both “Ga - Zr” and “Nb - Th” elements

in the region of $M_r = 2.2 - 5.9 M_\odot$. The first bump, located at $M_r = 2.0 - 3.6 M_\odot$, corresponds to the C, Ne, and O burning shells, while the second bump, found at $M_r = 5.0 - 5.9 M_\odot$, is associated with He shell burning. Between these two bumps, X (Ga-Zr) decreases due to low α production in the unburned regions.

In Figure 10, the distribution of ^{21}Ne is similar to the “Ga - Zr” elements, while ^{22}Ne displays an opposite trend. Compared to the unburned shells, there are more ^4He produced in the burning shells, which can consume ^{22}Ne and release more neutrons. New $^{22}\text{Ne}+\alpha$ reaction rates enhance X (Ga-Zr) only in the first bump, whereas the new $^{17}\text{O}+\alpha$ reaction rates positively affect X (Ga-Zr) across all the ws-process regions. Additionally, the new $^{17}\text{O}+\alpha$ reaction rates increase X (Nb - Th) by 50%, unlike the $^{22}\text{Ne}+\alpha$ reaction rates since these elements are produced during He burning stage. Notably, the sharp peak observed at $M_r = 1.84 - 2.0 M_\odot$ remains unaffected by both the $^{22}\text{Ne}+\alpha$ and $^{17}\text{O}+\alpha$ reaction rates, as these “Ga - Zr” elements are generated through the NSE process.

In this section, we follow the variation of the ws-process isotopes throughout the stellar evolution history and their mass distribution at the final stage for various reaction recipes. We find both new $^{22}\text{Ne}+\alpha$ and $^{17}\text{O}+\alpha$ reaction rates increase the production of the ws-process isotopes.

(1) The new $^{17}\text{O}+\alpha$ reaction rates only increase neutron density by ~ 3 times during He and C burning stages. On the contrary, the new $^{22}\text{Ne}+\alpha$ reaction rates increase the neutron density by several tens times during C and Ne burning stages.

(2) The new $^{17}\text{O}+\alpha$ reaction rates doesn’t vary the contribution in each burning stage. On the contrary, new $^{22}\text{Ne}+\alpha$ reaction rates significantly increase contribution in C and Ne burning stages, but decrease that in He burning stage.

(3) Before the explosion, the ws-process isotopes are primarily concentrated in the burning shells, with their abundances decreasing in the outer layers of the CO core. This is because there is no C burning in the outer layers of the CO core so that little ^4He is released.

4.2. The Integrated Yields

As indicated in Figure 7, the ws-process isotopes produced between the mass cut and the top of He burning shell may contribute to the overall enhancement. We integrate all the isotopes in this region rather than the entire star. We assume that the modifications of the ws-process yields in explosive nucleosynthesis can be ig-

nored and that all the radioactive isotopes decay into stable ones after the explosion. To investigate the sensitivity on the reaction rates, such approximations are reasonable.

In Figure 11 and 12, we show the ratios between the yields with new reaction rates ($\text{yield}_{\text{new}}$) and those with default reaction rates ($\text{yield}_{\text{def}}$) for $M(\text{ZAMS}) = 15, 20, 25$ and $30 M_\odot$, respectively.

(1) From C to Zn: With the new $^{22}\text{Ne}+\alpha$ reaction rates, we observe the increase in the yields of several neutron-rich isotopes of Ne, Mg, Si, S, Ar, and Ca, particularly those in ^{25}Mg , $^{29,30}\text{Si}$, ^{36}S , ^{40}Ar and ^{46}Ca . In Figure 14 (b), the significant decrease in the $^{22}\text{Ne}(\alpha, \gamma)^{26}\text{Mg}$ reaction rate at $T \simeq 1.5 - 2.0$ GK (during Ne burning) reduces the yield of ^{26}Mg . As a result, a greater amount of ^{22}Ne is converted to ^{25}Mg , leading to a significant increase in neutron production during Ne burning. Consequently, the yields of $^{21,22}\text{Ne}$ increase due to neutron capture on ^{20}Ne . Similarly, some $^{29,30}\text{Si}$ and most of the rare isotopes ^{36}S , ^{40}Ar and ^{46}Ca are also produced in Ne burning shell (Woosley & Weaver 1995). On the contrary, the new $^{17}\text{O}+\alpha$ reaction rates do not increase neutrons in the Ne shell, thus leaving the yields of those isotopes unchanged. The iron peak isotopes remain unaffected by both new $^{17}\text{O}+\alpha$ and $^{22}\text{Ne}+\alpha$ reaction rates, as they are primarily produced by the NES process at $M_r \simeq 1.8 - 2.2 M_\odot$, which is affected by Y_e . However, Y_e is only altered by the weak interaction.

(2) From Ga to Zr: Isotopes in this range are most significantly changed by the new reaction rates. The effect of the new $^{17}\text{O}+\alpha$ rates significantly differs from that of the new $^{22}\text{Ne}+\alpha$ reaction rates. For the same element, the increases due to the new $^{17}\text{O}+\alpha$ reaction rates in the isotopic yields are similar. However, for the new $^{22}\text{Ne}+\alpha$ reaction rates, the yields of some isotopes with fewer neutrons are reduced. With enriched neutrons, the isotopic yields increase quickly. As $M(\text{ZAMS})$ increases, the enhancement due to the new $^{17}\text{O}+\alpha$ reaction rates also increases, while the enhancement due to the new $^{17}\text{O}+\alpha$ reaction rates is not obviously affected by $M(\text{ZAMS})$.

(3) From Mo to Bi Isotopes in this range are not significantly altered by the new reaction rates. The new $^{22}\text{Ne}+\alpha$ reaction rates increase the yields of only a few isotopes for $M(\text{ZAMS}) = 15 M_\odot$ models. The number of such isotopes increases only slightly for more massive models.

In principle, the abundance of elements in the solar system arises from the cumulative contributions of numerous generations of stars with varying metallicities. Typ-

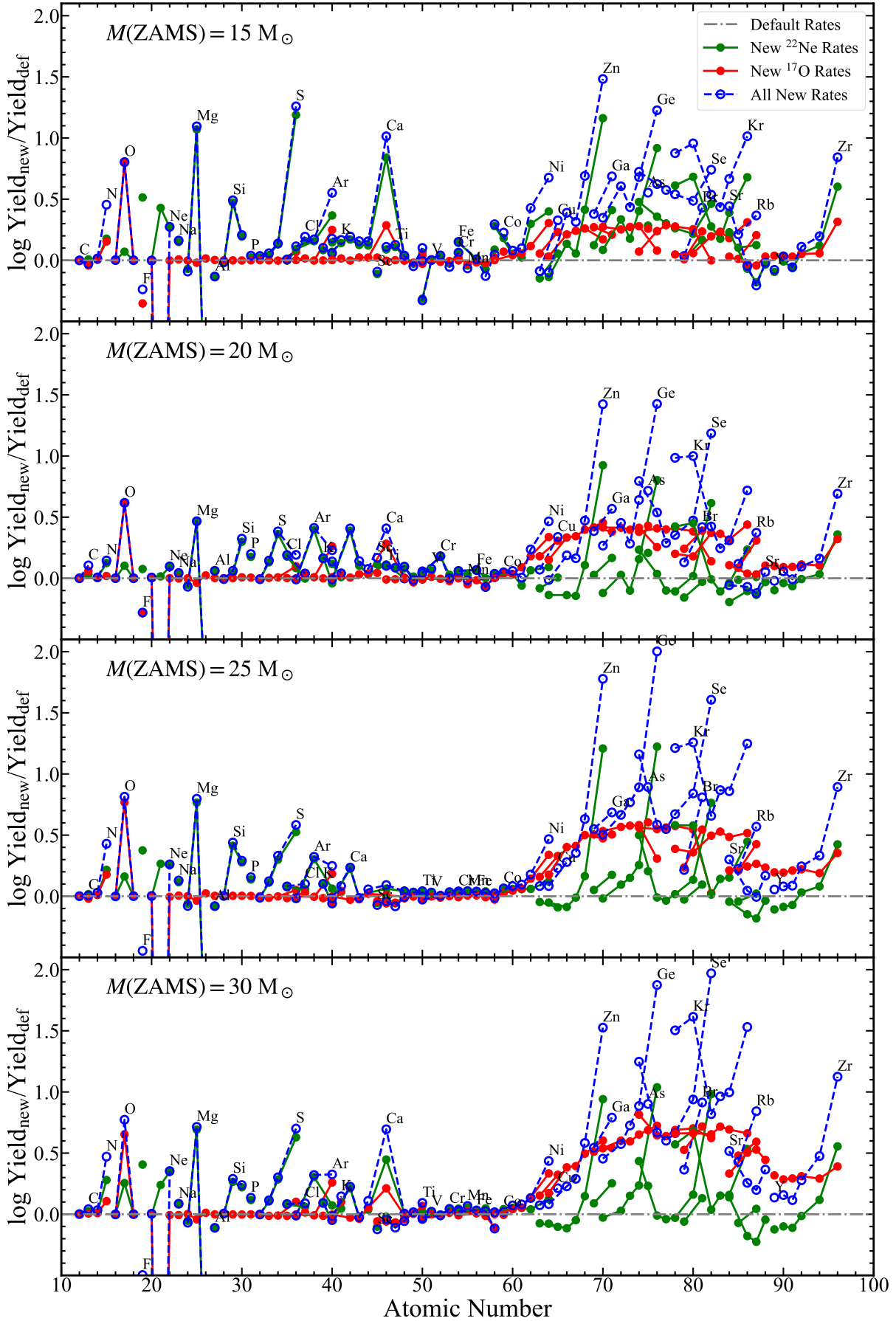


Figure 11. The ratios of isotopic yields (from C to Zr) between new rates and default rates for $M(\text{ZAMS}) = 15, 20, 25$ and $30 M_{\odot}$, respectively.

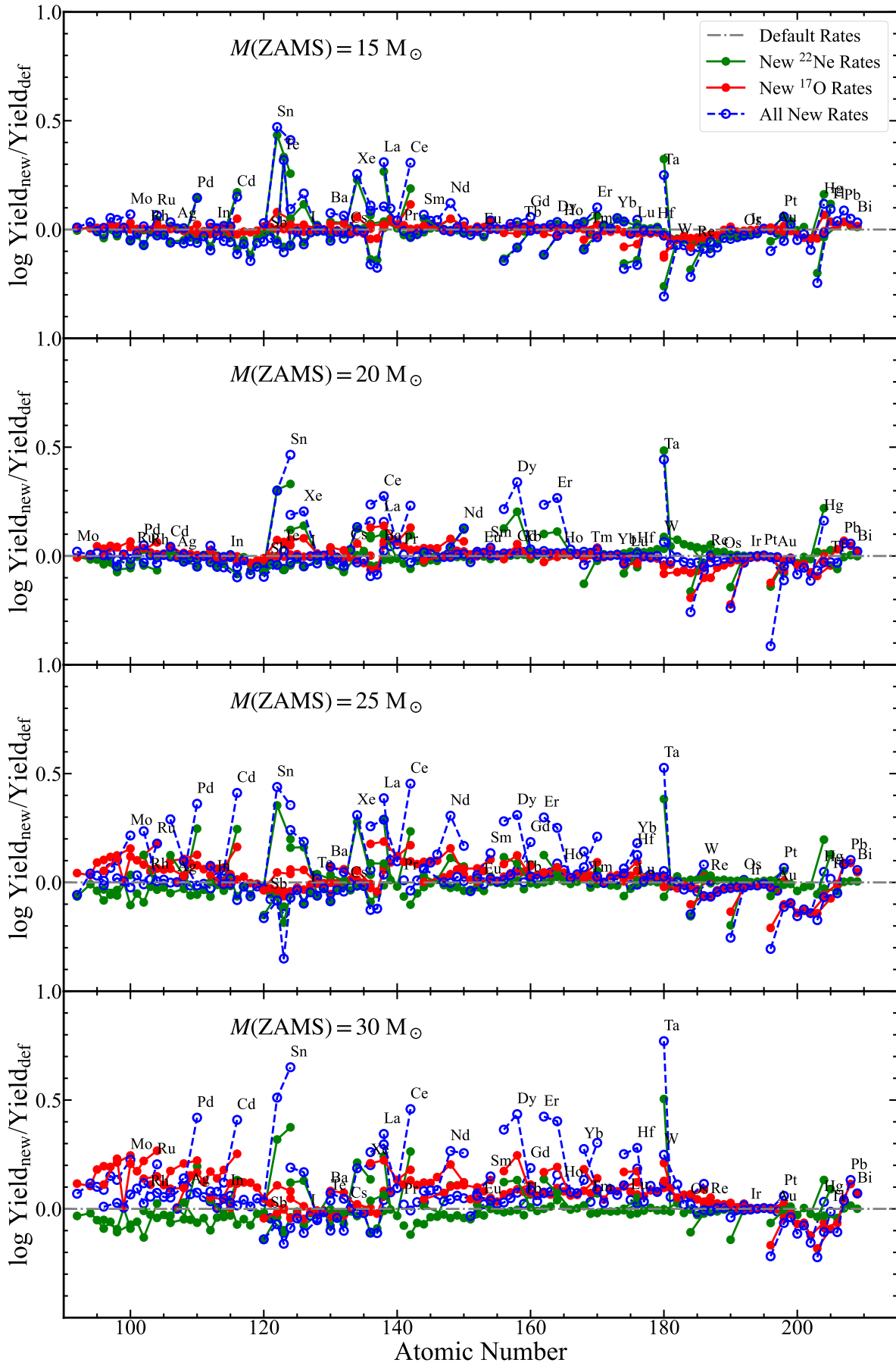


Figure 12. Same as Figure 11, but for elements from Mo to Bi.

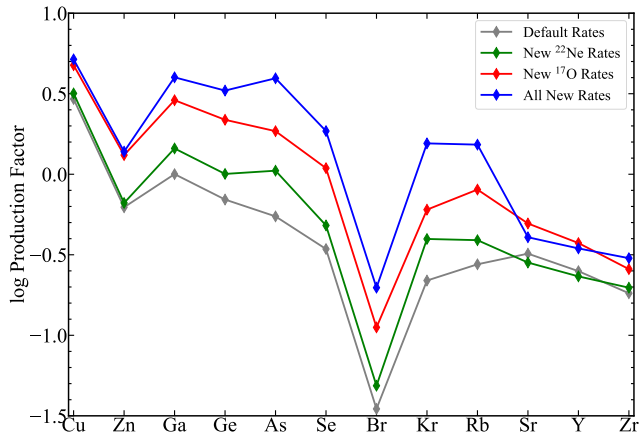


Figure 13. The production factors of the elements from Cu to Zr. Each element is integrated from 15 to 30 M_{\odot} with the Salpeter IMF with $\gamma = -2.35$.

ically, the stars in the range $0.1Z_{\odot} < Z < Z_{\odot}$ contribute more than 90% to the solar abundance (Limongi & Chieffi 2003). It is generally to use the production factors (PFs) to see which element is contributed significantly by a generation of stars. The PF of element i is defined as follows.

$$P_i \equiv \frac{Y_i^*}{X_{i\odot} \cdot \sum_k Y_k^*}, \quad (2)$$

where $X_{i\odot}$ denotes the solar mass fraction of element i . $\sum_k Y_k^*$ runs over all elements and Y_i^* represents the yield of element i averaged by the initial mass function (IMF) from Salpeter (1955) with $\gamma = -2.35$.

Figure 13 shows the production factors of the elements from Cu to Zr. Using the default and new $^{22}\text{Ne}+\alpha$ reaction rates, most elements are underproduced (green lines). However, when the new $^{17}\text{O}+\alpha$ reaction rates are included, the PFs from Zn to Rb increase by more than a factor of 0.5 dex. The contribution of stars with $0.1 Z_{\odot}$ to the solar abundance should be limited, as approximately 50% of the solar abundance is produced from stars with $0.5 Z_{\odot} < Z < Z_{\odot}$. Nevertheless, accounting for both new reaction rates leads to overproduction of Ga, Ge, As, and Se. Therefore, it is worth calculating the models with $0.5 Z_{\odot}$ and Z_{\odot} and verify whether the predictions concerning these elements align with observational data. Given the considerable uncertainties involved, it is essential to enhance the measurement accuracy of the (α, n) reaction rate, especially for the $^{17}\text{O}+\alpha$ reactions.

5. DISCUSSION

The primary purpose of this work is to evaluate the effect of the new $^{22}\text{Ne}+\alpha$ and $^{17}\text{O}+\alpha$ reaction rates. However, the size of the nuclear network used in MESA is limited

to ~ 300 isotopes, which makes it challenging to cover all the s-process isotopes. Therefore, the evolution and trajectories are based on the MESA calculation but the detailed nucleosynthesis is based on WinNet. In this section, we will discuss some uncertainties related to our calculation.

5.1. The Effect of Mixing

Nucleosynthesis in each zone is calculated separately because WinNet is a one-zone code. Thus, the effect of convective mixing is not taken into consideration. The mixing affects our results mainly in two aspects. On one hand, as seen in Figure 10, ^{22}Ne and ^{17}O are exhausted only in burning shells in the CO core, because the abundance of α particles are quite small in the unburned shells. While in Figure 4 from $M_r = 2.5 - 5.1 M_{\odot}$, mixing can transport ^{22}Ne and ^{17}O from unburned shells to the burning shells. As a result, more neutrons should be released in MESA calculation. Similarly, ^{17}O left in Figure 4 is quite small.

The convective mixing can also affect the locations of C, Ne, O, and Si burning shell. With mixing, more fresh fuels are transported from the outer layers to the bottom of the burning shells. The life of burning shells should be longer. Thus, the bottom of O shell burning located at $M_r = 1.84 M_{\odot}$ in Figure 4, while it moves to $M_r = 2.10 M_{\odot}$ in Figure 10. Similarly, the bases of the C and Ne shells are at $M_r = 2.0 M_{\odot}$, but shift to $M_r = 2.6$ and $2.7 M_{\odot}$ without mixing in WinNet.

5.2. The Effect of Explosion

As mentioned in Section 3.2, we assume that the mass cut locates at $M(V/U_{\text{max}})$ and the region of $M_r > M(V/U_{\text{max}})$ contributes to the chemical enrichment. We also assume that the ws-process isotopes produced in the explosive nucleosynthesis would be destroyed by the shock during the explosion. Thus, we don't calculate the explosive nucleosynthesis. The results from Tur et al. (2009) show that the explosive burning would reduce the ws-process isotopes by less than 15%. Limongi & Chieffi (2003) mentioned that for the isotopes of ^{70}Zn , ^{76}Ge , $^{74,77,82}\text{Se}$, ^{78}Kr , ^{87}Rb , ^{84}Sr , more than 50% of the yields are produced during explosive burning. These isotopes should be changed significantly by the shock wave. Since the exact explosion mechanism of core-collapse supernovae has not been well understood, the explosion energy and the choice of the mass cut will also affect the final yields of those isotopes.

5.3. Other Effects

Since the ws-process takes place mainly during the He, C, and Ne burning phases, The physical processes that

affect these burning phases may also affect the ws-process yields, such as reaction rates, convection, rotation, and magnetic fields (Hirschi 2023). Tur et al. (2009) have shown a 15% change in the 3α and $^{12}\text{C}(\alpha, \gamma)^{16}\text{O}$ reaction rates may change the yields of the ws-process isotopes by more than a factor of 2. Limongi & Chieffi (2018) presented a large number of rotating massive star models including the ws-process nucleosynthesis. Their models involve $M(\text{ZAMS}) = 13 - 120 M_{\odot}$ and metallicity of $-3 \leq [\text{Fe}/\text{H}] \leq 0$. They find the interplay between the He core and the H burning shell, which triggered by the rotation-induced instabilities, enhances the products of CNO (especially for ^{14}N) and produces more neutrons. As a result, the ws-process should be more significantly enhanced in rotating models.

6. CONCLUSION

In this work, we investigate the impact of new $^{17}\text{O}+\alpha$ reaction rates from Best et al. (2013) and new $^{22}\text{Ne}+\alpha$ reaction rates from Wiescher et al. (2023) in comparison to the default reaction rates in JINA REACLIB. We calculate nucleosynthesis of approximately 2000 isotopes, ranging from neutron and proton to thorium ($Z = 90$) using the one-zone code WinNet and the stellar models calculated with MESA for an initial metallicity of $Z = 0.1 Z_{\odot}$ and $M(\text{ZAMS}) = 15, 20, 25$ and $30 M_{\odot}$. All the models evolved from ZAMS to the Fe core collapse, where the infall speed of the Fe core reaches 10^8 cm/s. We assume that the corrections by explosive nucleosynthesis to the yields are minor and the isotopes lying outer of the mass cut ($M_r > M(V/U_{\text{max}})$) would contribute to the chemical enrichment of the Galaxy. The results are summarized as follows.

(1) The new $^{22}\text{Ne}+\alpha$ reaction rates slightly suppress the ws-process during He burning, while the new $^{17}\text{O}+\alpha$ reaction rates have the opposite effect. Both of them enhance the ws-process significantly during C burning and Ne burning. Using the reaction recipes listed in Table 1, X (Ga-Zr) increases by a factor of 6.56, 23.77, 31.58 and 113.62, respectively, after Ne burning (see Figure 8).

(2) We note that without considering the effect of mixing, the mass distribution of the ws-process isotopes pro-

vided by WinNet shows a two-bump shape (see Figure 9). This is because the unburned layers release fewer neutrons than the burning shells. This results in the underestimation of the yields of the ws-process isotopes. If nucleosynthesis of the ws-process is calculated, coupling with evolution instead of post-processing, the enhancement of the ws-process should be more significant.

(3) The new $^{17}\text{O}+\alpha$ reaction rates can increase the yields of all isotopes from Cu and Zr with the enhancement being more pronounced in more massive stars. Conversely, the new reaction rates for $^{22}\text{Ne}+\alpha$ only significantly enhance the yields of the most neutron-rich isotopes (see Figure 11).

(4) We average these four initial masses with Salpeter's IMF and show the production factors (PFs) of the elements from Cu to Zr. The new $^{17}\text{O}+\alpha$ reaction rates enhance the PFs more significantly than the new $^{22}\text{Ne}+\alpha$ reaction rates, especially, for Ga, Ge, As and Se. Considering such a significant impact that the reaction rates from Best et al. (2013) and JINA REACLIB have on the PFs of these elements, it is crucial to improve the accuracy and reliability of the measurement of the $^{17}\text{O}+\alpha$ reaction rates. Additionally, further investigations are necessary to ascertain which reaction rate can explain the astronomical observations well.

7. ACKNOWLEDGEMENTS

This work was supported by grants 12473028, 12073006, 12090040 and 12090042 from the National Natural Science Foundation of China. W. Y. X. is supported by the Cultivation Project for LAMOST Scientific Pay-off and Research Achievement. C. M. Y. is supported by grants from the Research Grant Council of the Hong Kong Special Administrative Region, China (Project Nos. 14300320 and 14304322) and the European Union through ERC Synergy Grant HeavyMetal no. 101071865. K. N. is supported by the World Premier International Research Center Initiative (WPI), MEXT, Japan, and the Japan Society for the Promotion of Science (JSPS) KAKENHI grants 20K04024, 21H04499, 23K03452, and 25K01046.

APPENDIX

A. REACTION RATES FROM REFERENCES

REFERENCES

- Anders, E., & Grevesse, N. 1989, *Geochimica et Cosmochimica Acta*, 53, 197, doi: [10.1016/0016-7037\(89\)90286-X](https://doi.org/10.1016/0016-7037(89)90286-X)
- Aoki, W., Honda, S., Beers, T. C., et al. 2005, *ApJ*, 632, 611, doi: [10.1086/432862](https://doi.org/10.1086/432862)

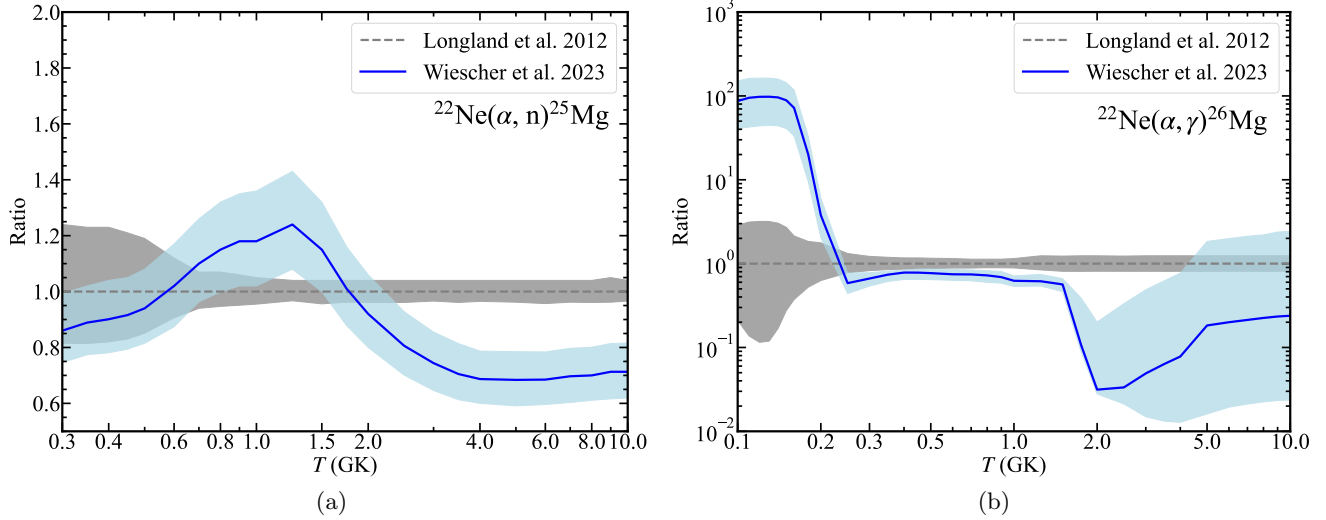


Figure 14. $^{22}\text{Ne}(\alpha, n)^{25}\text{Mg}$ and $^{22}\text{Ne}(\alpha, \gamma)^{26}\text{Mg}$ reaction rates from different references. The blue line and light-blue shaded region represent the recommended reaction rate and uncertainties from Wiescher et al. (2023). The gray dashed line and gray region represent the recommended reaction rate and uncertainties from Longland et al. (2012), which is adopted in JINA REACLIB database. To show the difference, all the data shown here is normalized by the recommended reaction rate from Longland et al. (2012).

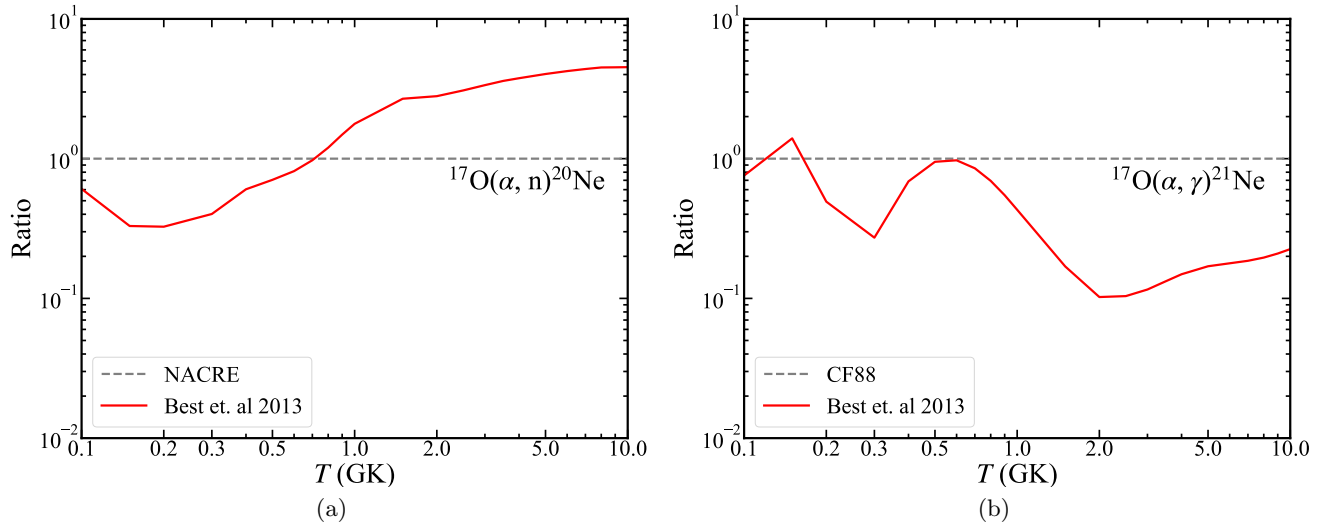


Figure 15. $^{17}\text{O}(\alpha, n)^{20}\text{Ne}$ and $^{17}\text{O}(\alpha, \gamma)^{21}\text{Ne}$ reaction rates from different references. The red line represents the recommended reaction rate from Best et al. (2013), which is normalized by the default the reaction rate in JINA REACLIB. The $^{17}\text{O}(\alpha, n)^{20}\text{Ne}$ and $^{17}\text{O}(\alpha, \gamma)^{21}\text{Ne}$ reaction rates used in JINA REACLIB come from NACRE database and CF88 database, respectively.

Aoki, W., Frebel, A., Christlieb, N., et al. 2006, *ApJ*, 639, 897, doi: [10.1086/497906](https://doi.org/10.1086/497906)

Arnett, W. D., & Thielemann, F. K. 1985, *ApJ*, 295, 589, doi: [10.1086/163402](https://doi.org/10.1086/163402)

Arnett, W. D., & Truran, J. W. 1969, *ApJ*, 157, 339, doi: [10.1086/150072](https://doi.org/10.1086/150072)

Baraffe, I., El Eid, M. F., & Prantzos, N. 1992, *A&A*, 258, 357

Best, A., Beard, M., Görres, J., et al. 2013, *PhRvC*, 87, 045805, doi: [10.1103/PhysRevC.87.045805](https://doi.org/10.1103/PhysRevC.87.045805)

Chiappini, C., Frischknecht, U., Meynet, G., et al. 2011, *Nature*, 472, 454, doi: [10.1038/nature10000](https://doi.org/10.1038/nature10000)

Chopin, A., Hirschi, R., Meynet, G., et al. 2018, *A&A*, 618, A133, doi: [10.1051/0004-6361/201833283](https://doi.org/10.1051/0004-6361/201833283)

Couch, R. G., Schmiedekamp, A. B., & Arnett, W. D. 1974, *ApJ*, 190, 95, doi: [10.1086/152851](https://doi.org/10.1086/152851)

Cyburt, R. H., Amthor, A. M., Ferguson, R., et al. 2010, *ApJS*, 189, 240, doi: [10.1088/0067-0049/189/1/240](https://doi.org/10.1088/0067-0049/189/1/240)

Farag, E., Renzo, M., Farmer, R., Chidester, M. T., & Timmes, F. X. 2022, *ApJ*, 937, 112,

doi: [10.3847/1538-4357/ac8b83](https://doi.org/10.3847/1538-4357/ac8b83)

- Farmer, R., Fields, C. E., Petermann, I., et al. 2016, *ApJS*, 227, 22, doi: [10.3847/1538-4365/227/2/22](https://doi.org/10.3847/1538-4365/227/2/22)
- Farmer, R., Laplace, E., Ma, J.-z., de Mink, S. E., & Justham, S. 2023, *ApJ*, 948, 111, doi: [10.3847/1538-4357/acc315](https://doi.org/10.3847/1538-4357/acc315)
- Frischknecht, U., Hirschi, R., & Thielemann, F. K. 2012, *A&A*, 538, L2, doi: [10.1051/0004-6361/201117794](https://doi.org/10.1051/0004-6361/201117794)
- Hayashi, C., Hōshi, R., & Sugimoto, D. 1962, *Progress of Theoretical Physics Supplement*, 22, 1, doi: [10.1143/PTPS.22.1](https://doi.org/10.1143/PTPS.22.1)
- Heger, A., & Woosley, S. E. 2010, *ApJ*, 724, 341, doi: [10.1088/0004-637X/724/1/341](https://doi.org/10.1088/0004-637X/724/1/341)
- Hirschi, R. 2023, *Slow Neutron-Capture Process in Evolved Stars*, ed. I. Tanihata, H. Toki, & T. Kajino (Singapore: Springer Nature Singapore), 3537–3571, doi: [10.1007/978-981-19-6345-2_118](https://doi.org/10.1007/978-981-19-6345-2_118)
- Hirschi, R., Frischknecht, U., Pignatari, M., et al. 2008, in *Nuclei in the Cosmos (NIC X)*, E83, doi: [10.22323/1.053.0083](https://doi.org/10.22323/1.053.0083)
- Hoffman, R. D., Woosley, S. E., & Weaver, T. A. 2001, *ApJ*, 549, 1085, doi: [10.1086/319463](https://doi.org/10.1086/319463)
- Jermyn, A. S., Bauer, E. B., Schwab, J., et al. 2023, *ApJS*, 265, 15, doi: [10.3847/1538-4365/aca8d](https://doi.org/10.3847/1538-4365/aca8d)
- Kappeler, F., Beer, H., & Wisshak, K. 1989, *Reports on Progress in Physics*, 52, 945, doi: [10.1088/0034-4885/52/8/002](https://doi.org/10.1088/0034-4885/52/8/002)
- Kippenhahn, R., Weigert, A., & Weiss, A. 2013, *Stellar Structure and Evolution*, doi: [10.1007/978-3-642-30304-3](https://doi.org/10.1007/978-3-642-30304-3)
- Kravchuk, P. A., & Yakovlev, D. G. 2014, *PhRvC*, 89, 015802, doi: [10.1103/PhysRevC.89.015802](https://doi.org/10.1103/PhysRevC.89.015802)
- Langanke, K., & Martínez-Pinedo, G. 2001, *Atomic Data and Nuclear Data Tables*, 79, 1, doi: [10.1006/adnd.2001.0865](https://doi.org/10.1006/adnd.2001.0865)
- Langer, N., Arcoragi, J. P., & Arnould, M. 1989, *A&A*, 210, 187
- Limongi, M., & Chieffi, A. 2003, *ApJ*, 592, 404, doi: [10.1086/375703](https://doi.org/10.1086/375703)
- Limongi, M., & Chieffi, A. 2018, *The Astrophysical Journal Supplement Series*, 237, 13, doi: [10.3847/1538-4365/aacb24](https://doi.org/10.3847/1538-4365/aacb24)
- Longland, R., Iliadis, C., & Karakas, A. I. 2012, *Phys. Rev. C*, 85, 065809, doi: [10.1103/PhysRevC.85.065809](https://doi.org/10.1103/PhysRevC.85.065809)
- Meyer, B. S., Weaver, T. A., & Woosley, S. E. 1995, *Meteoritics*, 30, 325, doi: [10.1111/j.1945-5100.1995.tb01131.x](https://doi.org/10.1111/j.1945-5100.1995.tb01131.x)
- Nishimura, N., Hirschi, R., Rauscher, T., St. J. Murphy, A., & Cescutti, G. 2017, *MNRAS*, 469, 1752, doi: [10.1093/mnras/stx696](https://doi.org/10.1093/mnras/stx696)
- Ohkubo, T., Nomoto, K., Umeda, H., Yoshida, N., & Tsuruta, S. 2009, *ApJ*, 706, 1184, doi: [10.1088/0004-637X/706/2/1184](https://doi.org/10.1088/0004-637X/706/2/1184)
- Osaki, Y. 1966, *PASJ*, 18, 384
- Paxton, B., Bildsten, L., Dotter, A., et al. 2011, *ApJS*, 192, 3, doi: [10.1088/0067-0049/192/1/3](https://doi.org/10.1088/0067-0049/192/1/3)
- Paxton, B., Cantiello, M., Arras, P., et al. 2013, *ApJS*, 208, 4, doi: [10.1088/0067-0049/208/1/4](https://doi.org/10.1088/0067-0049/208/1/4)
- Paxton, B., Marchant, P., Schwab, J., et al. 2015, *ApJS*, 220, 15, doi: [10.1088/0067-0049/220/1/15](https://doi.org/10.1088/0067-0049/220/1/15)
- Paxton, B., Schwab, J., Bauer, E. B., et al. 2018, *ApJS*, 234, 34, doi: [10.3847/1538-4365/aaa5a8](https://doi.org/10.3847/1538-4365/aaa5a8)
- Paxton, B., Smolec, R., Schwab, J., et al. 2019, *ApJS*, 243, 10, doi: [10.3847/1538-4365/ab2241](https://doi.org/10.3847/1538-4365/ab2241)
- Peters, J. G. 1968, *ApJ*, 154, 225, doi: [10.1086/149753](https://doi.org/10.1086/149753)
- Pignatari, M., Gallino, R., Heil, M., et al. 2010, *ApJ*, 710, 1557, doi: [10.1088/0004-637X/710/2/1557](https://doi.org/10.1088/0004-637X/710/2/1557)
- Prantzos, N., Hashimoto, M., & Nomoto, K. 1990, *A&A*, 234, 211
- Raiteri, C. M., Busso, M., Gallino, R., & Picchio, G. 1991a, *ApJ*, 371, 665, doi: [10.1086/169932](https://doi.org/10.1086/169932)
- Raiteri, C. M., Busso, M., Gallino, R., Picchio, G., & Pulone, L. 1991b, *ApJ*, 367, 228, doi: [10.1086/169622](https://doi.org/10.1086/169622)
- Raiteri, C. M., Gallino, R., & Busso, M. 1992, *ApJ*, 387, 263, doi: [10.1086/171078](https://doi.org/10.1086/171078)
- Raiteri, C. M., Gallino, R., Busso, M., Neuberger, D., & Kaeppler, F. 1993, *ApJ*, 419, 207, doi: [10.1086/173476](https://doi.org/10.1086/173476)
- Rauscher, T., Heger, A., Hoffman, R. D., & Woosley, S. E. 2002, *ApJ*, 576, 323, doi: [10.1086/341728](https://doi.org/10.1086/341728)
- Reichert, M., Winteler, C., Korobkin, O., et al. 2023, *ApJS*, 268, 66, doi: [10.3847/1538-4365/acf033](https://doi.org/10.3847/1538-4365/acf033)
- Salpeter, E. E. 1955, *ApJ*, 121, 161, doi: [10.1086/145971](https://doi.org/10.1086/145971)
- Schwarzschild, M. 2015, *Structure and Evolution of Stars*, doi: [10.1515/9781400879175](https://doi.org/10.1515/9781400879175)
- Sugimoto, D., & Nomoto, K. 1980, *SSRv*, 25, 155, doi: [10.1007/BF00212318](https://doi.org/10.1007/BF00212318)
- Sukhbold, T., Ertl, T., Woosley, S. E., Brown, J. M., & Janka, H. T. 2016, *ApJ*, 821, 38, doi: [10.3847/0004-637X/821/1/38](https://doi.org/10.3847/0004-637X/821/1/38)
- The, L. S., El Eid, M. F., & Meyer, B. S. 2000, *ApJ*, 533, 998, doi: [10.1086/308677](https://doi.org/10.1086/308677)
- The, L.-S., El Eid, M. F., & Meyer, B. S. 2007, *ApJ*, 655, 1058, doi: [10.1086/509753](https://doi.org/10.1086/509753)
- Timmes, F. X., & Arnett, D. 1999, *ApJS*, 125, 277, doi: [10.1086/313271](https://doi.org/10.1086/313271)
- Tur, C., Heger, A., & Austin, S. M. 2009, *ApJ*, 702, 1068, doi: [10.1088/0004-637X/702/2/1068](https://doi.org/10.1088/0004-637X/702/2/1068)
- Weaver, T. A., Zimmerman, G. B., & Woosley, S. E. 1978, *ApJ*, 225, 1021, doi: [10.1086/156569](https://doi.org/10.1086/156569)

- Wiescher, M., deBoer, R. J., & Görres, J. 2023, *European Physical Journal A*, 59, 11,
doi: [10.1140/epja/s10050-023-00917-9](https://doi.org/10.1140/epja/s10050-023-00917-9)
- Woesley, S. E., & Heger, A. 2007, *PhR*, 442, 269,
doi: [10.1016/j.physrep.2007.02.009](https://doi.org/10.1016/j.physrep.2007.02.009)
- Woesley, S. E., Heger, A., & Weaver, T. A. 2002, *Reviews of Modern Physics*, 74, 1015,
doi: [10.1103/RevModPhys.74.1015](https://doi.org/10.1103/RevModPhys.74.1015)
- Woesley, S. E., & Weaver, T. A. 1995, *ApJS*, 101, 181,
doi: [10.1086/192237](https://doi.org/10.1086/192237)
- Xin, W., Nomoto, K., & Zhao, G. 2025, arXiv e-prints,
arXiv:2502.11012, doi: [10.48550/arXiv.2502.11012](https://doi.org/10.48550/arXiv.2502.11012)